Role of laser contrast and foil thickness in target normal sheath acceleration

L.A. Gizzi [a,b], C. Altana [c,d], F. Brandi [a,e], P. Cirrone [d], G. Cristoforetti [a], A. Fazzi [f,g], P. Ferrara [a],
L. Fulgentini [a], D. Giove [h], P. Koester [a], L. Labate [a,b], G. Lanzalone [d,i], P. Londrillo [m],
D. Mascali [d], A. Muoio [d], D. Palla [a,b,l], F. Schillaci [d], S. Sinigardi [j,k], S. Tudisco [d], G. Turchetti [j,k]

[a] *ILIL, Istituto Nazionale di Ottica, CNR, Via G. Moruzzi 1, Pisa, Italy*
[b] *INFN Sezione di Pisa, Largo Pontecorvo 3, 56127 Pisa, Italy*
[c] *Dipartimento di Fisica e Astronomia, Università degli Studi di Catania, Italy*
[d] *Laboratori Nazionali del Sud, INFN, Via S. Sofia, Catania, Italy*
[e] *Istituto Italiano di Tecnologia, Via Morego 30, 16163 Genova, Italy*
[f] *Energy Department, Polytechnic of Milan, Milan, Italy*
[g] *INFN, Milan, Italy*
[h] *INFN-LASA, Via Fratelli Cervi 201, 20090 Segrate, Italy*
[i] *Università degli Studi di Enna Kore, Via delle Olimpiadi, 94100 Enna, Italy*
[j] *Dipartimento di Fisica e Astronomia, Università di Bologna, Bologna, Italy*
[k] *INFN, Sez. di Bologna, Via Irnerio 46, 40126 Bologna, Italy*

[l] *Dipartimento di Fisica, Università di Pisa, Italy*
[m] *INAF–Osservatorio astronomico Bologna, Italy*

ARTICLE INFO

ABSTRACT

In this paper we present an experimental investigation of laser driven light-ion acceleration using the ILIL laser at an intensity of 2×10^{19} W/cm^2. In the experiment we focused our attention on the identification of the role of target thickness and resistivity in the fast electron transport and in the acceleration process. Here we describe the experimental results concerning the effect of laser contrast in the laser–target interaction regime. We also show preliminary results on ion acceleration which provide information about the role of bulk target ions and surface ions and target dielectric properties in the acceleration process.

1. Introduction

Novel acceleration techniques for protons and light ions, capable of accelerating gradients higher than those currently available, are highly desirable for the development of new, compact accelerators. Several mechanisms based on ultra-intense lasers have been identified and are being explored experimentally. Among these, Target Normal Sheath Acceleration (TNSA) [1] is certainly the most robust mechanism, which has been explored for a wide range of laser and target parameters and for target thickness down to tens of nanometers [2,3]. These experiments show that for relatively thin targets, down to a few micrometers, TNSA is reliable and relatively easy to implement even for a range of applications where rep-rated operation is required. Although a significant progress has been made in the identification of the key physical mechanisms behind the acceleration process, a full understanding of the process is still lacking, especially when considering the dependence on target parameters like resistivity and composition and, more recently, nanoscale structure.

Moreover, a satisfactory understanding of the dependence of maximum ion energy with target thickness [4] is still missing, due to the strong dependence of ion acceleration upon laser contrast [5] and target physical and geometrical properties [6]. Finally, more investigation is also needed to study the role of bulk target ions in the acceleration process compared to the ions originating from the target surface typical of TNSA. A systematic approach to all these issues may provide advanced solutions for further enhancement of ion energy and charge.

Here we describe the preliminary results of an experimental campaign on laser driven light ion acceleration established in the framework of a new initiative aimed at the construction of an all-optical accelerator line for light ions following the ongoing sub-PW upgrade of the ILIL laser. The first phase of the campaign was focused on the laser–plasma interaction physics, with special attention to the identification of spectroscopic features useful for an accurate characterisation of the quality of the interaction and to the fast electron generation and transport in the target. Particular attention was dedicated to the detection of the effect of the
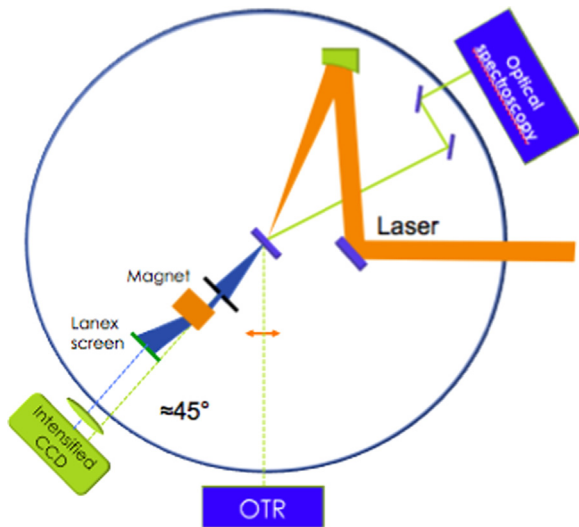
Fig. 1. Schematic view of the experimental setup showing the main diagnostics, including the optical spectroscopy of the specular reflection, the rear side optical imaging and the magnetic electron spectrometer of the forward escaping electrons. A Thomson Parabola ion spectrometer was used in place of the electron spectrometer to detect forward accelerated ions.
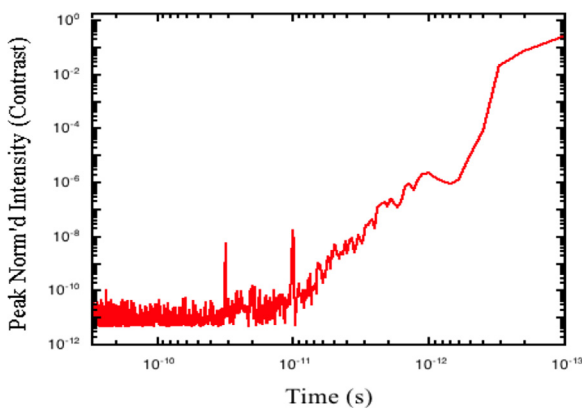
Fig. 2. Log–log plot of the measured laser contrast of the ILIL system. The sub-nanosecond ASE contrast is better that 10^9 up to 10 ps before the peak of the pulse and reaches 10^6 at 1 ps.

available laser contrast in the sub-nanosecond and picosecond temporal scale. Finally, preliminary measurements of the ion energy were carried out for a range of target thicknesses and materials.

2. The experimental setup

The experiment was carried out at the Intense Laser Irradiation Laboratory using the 10 TW Ti:Sa laser system which delivers up to 450 mJ on target and features an M^2 to 1.5. As shown schematically in Fig. 1, the laser was focused, at an angle of incidence of 15°, using an f/4.5 Off-Axis Parabolic mirror (OAP), in a spot size of 6.2 μm FWHM, giving a nominal intensity on target of about 2×10^{19} W/cm^2. The nanosecond temporal contrast of the pulse set by the Amplified Spontaneous Emission (ASE) was better than 10^{10}, thus enabling a pre-plasma free interaction with the solid target down to the picosecond temporal regime. In view of this, in the reminder of this paper we will refer to "pre-plasma" as the short scalelength plasma generated by the picosecond pedestal of the laser pulse, typically arising from imperfections of the pulse compression. In fact, as shown by the cross-correlation curve of

Fig. 2, the laser contrast remains better than 10^{10} up to 10 ps before the peak of the pulse and decreases to 10^6 at 1 ps before the peak of the pulse. Taking into account this temporal profile, we expect plasma formation to start not earlier than 10 ps before the peak of the pulse. In this case, the plasma formed in front of the solid target is expected to have a very steep density gradient [7]. In view of these observations, special attention was dedicated in the experimental campaign to monitor target integrity prior to the arrival of the main pulse on target.

We used optical spectroscopy of the light scattered in the specular direction to monitor generation of second harmonic emission, $2\omega_L$, and $(3/2)\omega_L$ of the incident laser light. These components of the scattered radiation are associated to the coupling of the laser light at the critical density and at the quarter critical density respectively [8]. The formation of even a very small pre-plasma before the arrival of the main pulse can provide suitable conditions for the growth of stimulated instabilities including the Stimulated Raman Scattering and the Two Plasmon Decay (see [7] and references therein). Electron plasma waves at $\omega_L/2$ generated by the instabilities can couple non-linearly with incident laser light and give rise to $(3/2)\omega_L$ emission. This emission is therefore a signature of the presence of even a small pre-plasma. On the other hand, second harmonic emission in the specular direction is generated by the non-linear interaction of the main laser pulse at the critical density [9]. Therefore, second harmonic emission can be taken as a signature of the presence of a critical density layer in the plasma at the time of interaction of the main pulse, a prerequisite for the interaction with an over-dense target and the occurrence of TNSA.

The behaviour of the interaction in our experimental conditions is revealed by the focal scan of the optical scattering in the specular direction, as shown in Fig. 3. When the target is significantly out of focus, more than three Rayleigh lengths from the best focus position, scattered radiation is dominated by $2\omega_L$, with very weak $(3/2)\omega_L$ emission, indicating negligible pre-plasma formation and target survival at the peak of the pulse. According to Fig. 3, as the target gets close to the best focus conditions and the laser intensity increases, the $(3/2)\omega_L$ emission intensity increases and broadens leading to a quasi-continuum emission from 400 nm up to 560 nm as observed previously in similar irradiation conditions [10]. A quantitative analysis of this spectrum is complex and is beyond the scope of this work. However, we can anticipate that this behaviour is indicative of a more efficient growth of the instability, possibly due to both the higher laser intensity and the longer density scale-length of the plasma. In spite of the increase of the $(3/2)\omega_L$ intensity, the intensity of the $2\omega_L$ emission remains significant, strongly suggesting that laser contrast in the best focus is sufficient to ensure survival of the target. These conclusions are consistent with hydrodynamic numerical simulations performed in similar experimental conditions [7] to evaluate the role of the pre-pulse intensity on the target as shown by the plot of Fig. 2. Simulations show that plasma density scale-length at a quarter critical density is as large as a few μm at the position of best focus and becomes smaller than the laser wavelength at distances from the best focus where $(3/2)\omega_L$ emission vanishes.

According to these observations, we expect that in our experimental conditions and with our laser contrast, targets with a thickness as small as a few μm should be considered, while great care should be taken when using targets with a thickness below 2–3 μm. Incidentally, we point out that this diagnostic technique, based on the spectroscopy of optical radiation scattered in the specular direction, provides a simple and effective monitor of the interaction and which is highly sensitive to both relative focusing conditions and picosecond contrast.
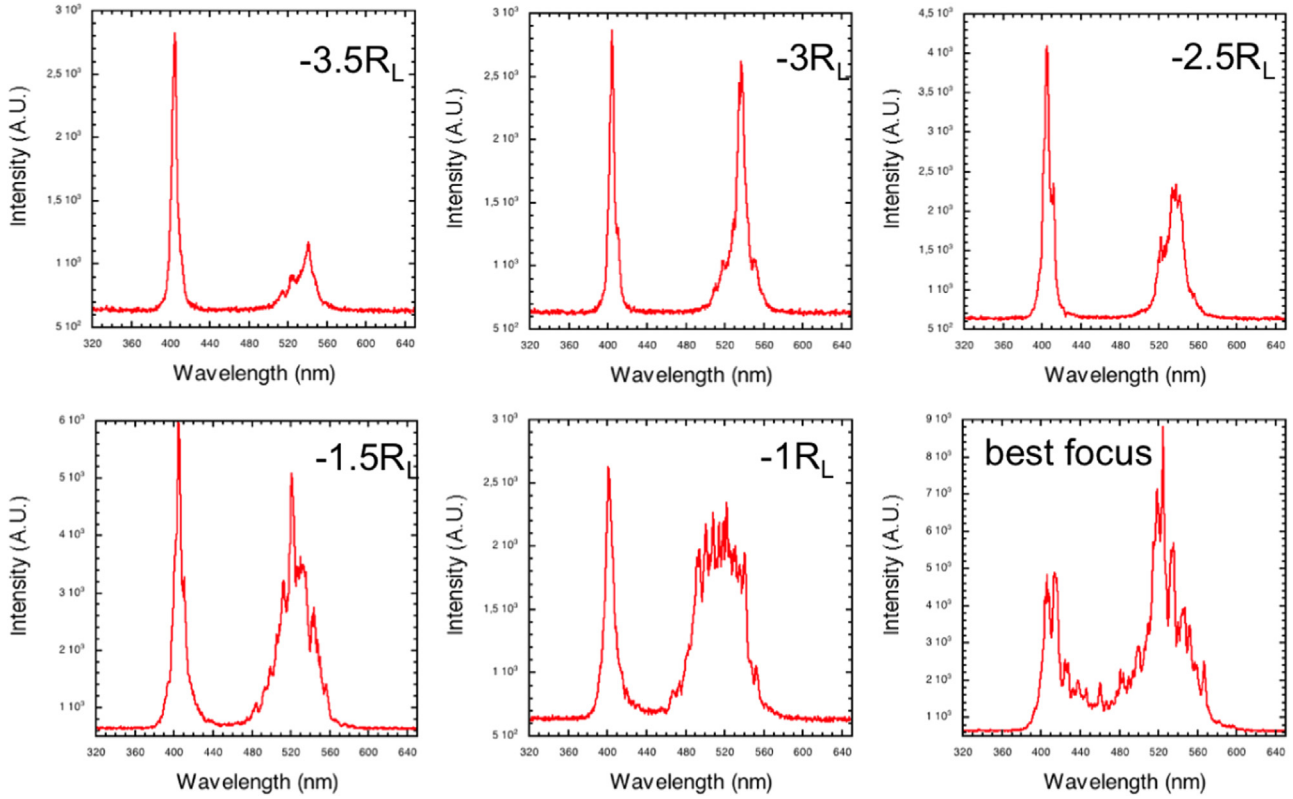
Fig. 3. Spectra of the optical radiation scattered along the specular direction of the incident laser. Different spectra are shown for a different position of the 30 μm thick Cu target along the focal axis, for distance from the best focus up to 3.5 Rayleigh lengths ($L_R = 50$ μm). The emission at 400 nm is due to second harmonic of the laser light occurring at the critical density, while the emission at $(3/2)\omega_L$ is due to the interaction at the quarter critical density.

3. Fast electron measurements

Given the key role played by fast electron generation and transport in TNSA acceleration, dedicated measurements were carried out to detect and characterise forward escaping fast electrons using a permanent magnet electron spectrometer with a detection range from 1 MeV to 5 MeV. Also, as shown in Fig. 1, optical imaging of the rear side of the target at 45° from the target normal was performed to detect Optical Transition Radiation (OTR) from electrons crossing the target rear surface. Measurements were carried out with the target placed either at the best focus position or 100 μm from the best focus towards the off-axis parabola. Clear forward electron emission was detected in the condition of best focus while no electron emission was detectable out of focus. These circumstances are confirmed by the rear side images which clearly show optical emission (OTR) strongly correlated with the forward escaping fast electrons. In addition, OTR images (not shown here) taken for different target materials and thicknesses exhibit similar spectral and angular properties. The correlation between best focus position and detectable forward electron emission could be explained by the observations on the optical spectroscopy of specular radiation which show a strong $(3/2)\omega_L$ component when the target is at the best focus position. In fact, the occurrence of strong $(3/2)\omega_L$ emission would imply the generation of electron plasma waves at $\omega_L/2$ due to Two Plasmon Decay which will give rise to a population of fast electrons with high directionality [7].
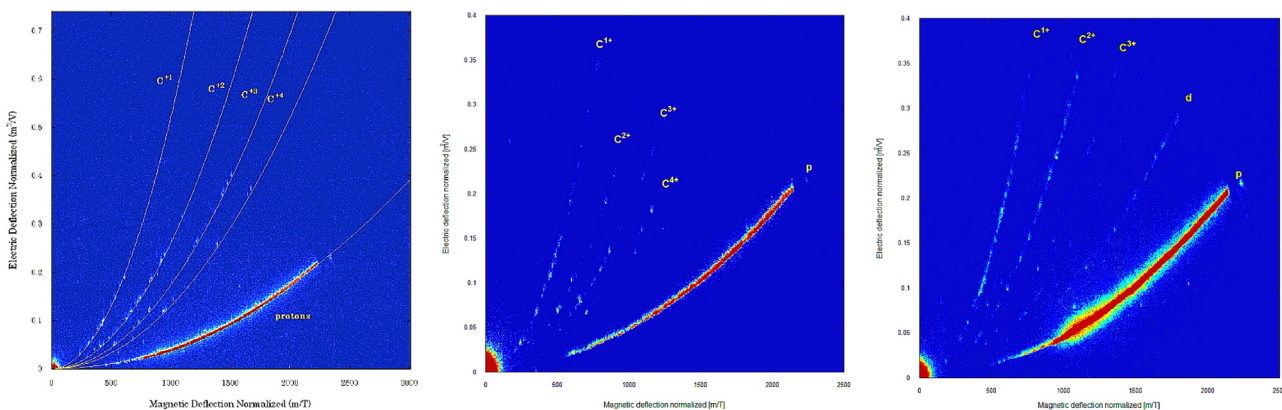
4. Ion detection

A range of diagnostics were used in our experiments to measure ion acceleration, including radio-chromic films (GAF), CR39, Thomson Parabola and a Time of Flight (TOF) diamond detectors. Normally, the Thomson Parabola and the Diamond detector were used simultaneously so that a cross comparison of the signals obtained from the two devices was possible. This was done in view of the possible use of the Diamond detector for on-line direct detection of accelerated ions. We used a stack of radiochromic films arranged to detect ions and forward emitted fast electrons and to reconstruct the energy distribution [11,12]. We used EBT3 Gafchromic films where the 120 μm thick polyester protective layer was removed to detect lower energy ions. In this way, protons with an energy down to about 1 MeV could be detected by the first EBT3 layer, the low energy cut-off being set by the 12 μm thick Al foil used to shield the RCF film from scattered laser light and debris. A typical ion pattern obtained on the first layer of the RCF stack from irradiation of a 10 μm thick Al foil is shown in Fig. 4 (left). As expected, the ion pattern is superimposed on a diffuse signal due to hot electrons co-propagating with the ions. Faint or no ions signal was visible on the second RCF layer which, according to SRIM [13] calculations, sets the high energy limit of detected protons to 3.8 MeV.

Fig. 4 (right) shows instead the signal obtained by the TOF diamond detector which was placed at a distance of 28 cm and was filtered using a 12 μm thick Al foil. The strong photo-peak, due to X-rays and fast electrons reaching the detector soon after the interaction, peaks at 6 ns, showing a rise time of approximately 2 ns, which can be taken as the overall response time of the detecting chain due to the bandwidth of the amplifier, the oscilloscope and the connecting cables. This photo-peak is followed by the ion signal which starts at 18 ns, namely 14 ns after the starting of the photo-peak. Taking into account the TOF distance and assuming a signal predominantly due to protons, calculations yield a maximum ion energy (high energy cut-off) of 1.9 MeV. These values are fully consistent with the GAF measurements discussed above.
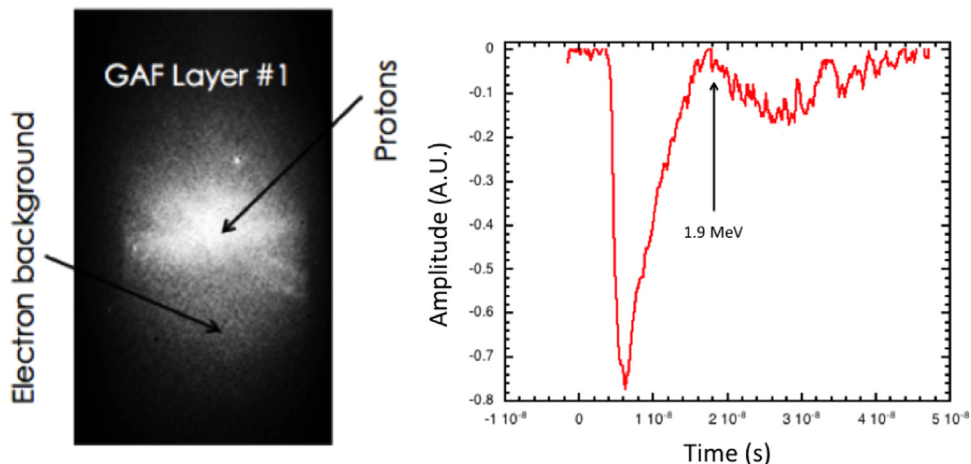
Fig. 4. (Left) Image of the GAF film after exposure to the ion accelerated beam obtained from irradiation of a 10 μm thick Al target. (Right) Signal of the Diamond detector corresponding to ions between 1.9 MeV and 0.8 MeV. $T=0$ is arbitrary in this plot.

Fig. 5. Typical raw output images of the Thomson Parabola ion detector, with arbitrary intensity scale, obtained by irradiation of a 10 μm thick foil (left), 4 μm thick CH_2 foil coated with 100 nm Al (centre), and 4 μm thick CD_2 foil coated with 100 nm Al (right). Clearly visible is the signal corresponding to accelerated protons. Signal from the four ionisation stages of Carbon ions is also visible.

A more accurate ion analysis was carried out using the Thomson Parabola. The TP was placed on the target rear side, in the direction of the target normal, at a distance of 129 cm from the target surface to micro-channel plate output. A detailed description of the TP used in this set of measurements is given elsewhere (see [14] and references therein).

A typical raw TP output is shown in Fig. 5 for three different targets. Fig. 5 (left) corresponds to a 10 μm thick Al target, showing the proton signal and also the signal from all ionisation stages of carbon ions. A much similar signal was obtained irradiating a 4 μm thick CH_2 target, coated with 100 nm Al, as shown in Fig. 5 (centre). Fig. 5 (right) shows instead the signal from irradiation of a 4 μm thick CD target, coated with 100 nm Al.

In this context, the use of CD_2 targets was demonstrated [15] to provide information about localisation of the accelerating field. In fact, targets can be arranged so that deuteron ions are available only in preset target locations and can be efficiently accelerated. In our experiment, the comparison between CH_2 and CD_2 targets with the same thickness enables us to add information on the role of bulk target ions, compared to ions in the target contaminant layer from which TNSA protons are primarily expected to originate. In fact, in the case of CD_2 target, the TP image clearly shows signal from deuterons, along with protons, confirming that deuterons, only available in the bulk of the target, are accelerated along with surface contaminant ions.

This simple technique is being considered to get a quantitative analysis of bulk ion acceleration in future experiments. In particular, the ion temperature parameter was found [14] to exhibit opposite trends upon the laser intensity across the focal position, suggesting a complex interplay between volume and surface acceleration.

A more comprehensive picture of the TNSA scenario in our experimental conditions can be gained by the plot of Fig. 6 which shows a summary of the proton cut-off energy obtained for CH_2 targets with thickness ranging from 6 μm to 23 μm and for Al targets with thickness ranging from 2 μm to 12 μm.

As a first comment, we notice that the maximum cut-off energy of 1.5 MeV ± 0.2 MeV is found for a target thickness around 12 μm of Al. We point out that Al target thickness greater than 12 μm was not explored and will be tested in future measurements. In the case of CH_2 a cut-off energy of 1.4 MeV ± 0.2 MeV was found. At this stage we can however say that our preliminary results are consistent with the preliminary GAF measurements and with the values expected from TNSA scaling laws [3].

In addition, we point out that both target types yield similar cut-off energy and a similar trend for thickness values of 6 μm and 12 μm, showing little dependence on the cold target dielectric properties. We recall here that no significant dependence upon target material was observed in OTR imaging, further suggesting that in our experimental conditions, cold target electron conductivity (target resistivity) does not play a significant role.

Moreover, we observe that in both cases, proton cut-off energy decreases rapidly with target thickness, with the proton cut-off energy at 2–3 μm being almost half of the cut-off energy at 6 μm.
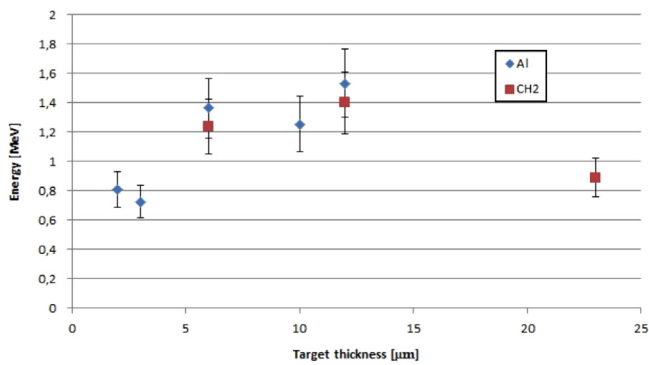
Fig. 6. Dependence of the cut-off proton energy measured in our experiments as a function of the target thickness for both metallic target (Al) and dielectric target (CH₂).

It is well known that the cut-off energy with thinner targets is mainly dependent upon the contrast of the laser pulse and can be strongly enhanced using contrast enhancement techniques like the plasma mirror [16,17]. In fact, the contrast at the picosecond level sets the spatial scale of the plasma at the time of the peak intensity, affecting the interaction and the fast electron production. As discussed above, the optical scattering spectra in the specular direction suggest that in our experimental conditions, at best focus, the pre-pulse intensity at the ps level indeed limits to 2–3 µm the minimum target thickness at which the pre-plasma is not sufficiently developed to prevent efficient TNSA. Although further investigation is needed to quantify the scale length of the pre-plasma, observation concerning the trend of the cut-off energy of Fig. 6 for target thickness below 5 µm is consistent with this picture.

5. Conclusion

In summary, we have carried out an investigation on ion acceleration in the TNSA regime, with special attention to the laser–target coupling and to the identification of signatures in optical spectroscopy and imaging of scattered light. Optical spectroscopy of light scattered in the specular direction provides useful insight in the laser-target energy coupling, showing features that can be associated to the generation of a µm sized density scale-length due to the picosecond pedestal of the laser pulse. Measurements of the ion acceleration show that these circumstances affect TNSA for target thickness below 2–3 µm. Optical Transition Radiation is detected in coincidence with the generation of a fast electron beam propagating in the forward direction. The dependence of the ion cut-off energy is found to be consistent with the expected scaling laws regardless of the target material being Al or plastic and is found to increase with target thickness in the explored thickness range up to 12 µm. All these experimental observations, although in a preliminary stage of analysis, provide a quite complete characterisation of the laser–target interaction regime in our experimental conditions and a reference set of data for the upcoming upgrade of the laser installation.

References

[1] R.A. Snavely, Physical Review Letters 85 (14) (2000) 2945, http://dx.doi.org/10.1103/PhysRevLett.85.2945.

[2] H. Daido, M. Nishiuchi, A.S. Pirozhkov, Reports on Progress in Physics 75 (5) (2012) 056401.

[3] A. Macchi, M. Borghesi, M. Passoni, Review of Modern Physics 85 (2013) 751.

[4] J. Lu, X. Lan, X. Xi, H. Zhang, J. Zhang, L. Wang, X. Tang, N. Wang, Plasma Science and Technology 17 (6) (2015) 458, http://dx.doi.org/10.1088/1009-0630/17/6/04, URL ⟨http://stacks.iop.org/1009-0630/17/i=6/a=458?key=crossref.cdd73f2a809af18cc0c011afe324883f⟩.

[5] M. Tayyab, S. Bagchi, B. Ramakrishna, T. Mandal, A. Upadhyay, R. Ramis, J.A. Chakera, P.A. Naik, P.D. Gupta, Physical Review E 90 (2014) 1, http://dx.doi.org/10.1103/PhysRevE.90.023103, URL ⟨http://link.aps.org/doi/10.1103/PhysRevE.90.023103⟩.

[6] T.Z. Esirkepov, J.K. Koga, A. Sunahara, T. Morita, M. Nishikino, K. Kageyama, H. Nagatomo, K. Nishihara, A. Sagisaka, H. Kotaki, T. Nakamura, Y. Fukuda, H. Okada, A.S. Pirozhkov, A. Yogo, M. Nishiuchi, H. Kiriyama, K. Kondo, M. Kando, S.V. Bulanov, Nuclear Instruments and Methods in Physics Research Section A: Accelerators, Spectrometers, Detectors and Associated Equipment 745 (2014) 150, http://dx.doi.org/10.1016/j.nima.2014.01.056, URL ⟨http://linkinghub.elsevier.com/retrieve/pii/S0168900214001077⟩.

[7] F. Baffigi, G. Cristoforetti, L. Fulgentini, A. Giulietti, P. Koester, L. Labate, L.A. Gizzi, Physics of Plasmas 21 (7) (2014) 072108, http://dx.doi.org/10.1063/1.4886977.

[8] L.A. Gizzi, Advances in X-ray studies of ultraintense laser–plasma interactions, in: K. Yamanouchi, A. Giulietti, K. Ledingham (Eds.), Progress in Ultrafast Intense Laser Science, vol. V, Springer Series in Chemical Physics, vol. 98, 2010, pp. 123–138.

[9] L.A. Gizzi, D. Giulietti, A. Giulietti, P. Audebert, S. Bastiani, J.P. Geindre, A. Mysyrowicz, Physical Review Letters 76 (13) (1996) 2278.

[10] L.A. Gizzi, A. Giulietti, D. Giulietti, P. Koester, L. Labate, T. Levato, F. Zamponi, T. Kämpfer, I. Uschmann, E. Förster, R. Sauerbrey, Optimization and control of bright, ultrafast laser driven X-ray sources, in: Proceedings of SPIE, vol. 6634, SPIE—International Society of Optical Engineering, Bellingham, Washington, USA, 2007.

[11] M. Galimberti, A. Giulietti, D. Giulietti, L.A. Gizzi, Review of Scientific Instruments 76 (2005) 053303.

[12] E. Breschi, M. Borghesi, M. Galimberti, D. Giulietti, L. Gizzi, L. Romagnani, Nuclear Instruments & Methods in Physics Research Section A—Accelerators, Spectrometers, Detectors and Associated Equipment 522 (2004) 190.

[13] ⟨http://www.srim.org/⟩.

[14] S. Tudisco, C. Altana, G. Lanzalone, A. Muoio, G.A.P. Cirrone, D. Mascali, F. Schillaci, F. Brandi, G. Cristoforetti, P. Ferrara, L. Fulgentini, P. Koester, L. Labate, D. Palla, L.A. Gizzi, Review of Scientific Instruments 87 (2) (2016) 02A909, http://dx.doi.org/10.1063/1.4934691.

[15] L. Willingale, G.M. Petrov, A. Maksimchuk, J. Davis, R.R. Freeman, T. Matsuoka, C.D. Murphy, V.M. Ovchinnikov, L. Van Woerkom, K. Krushelnick, Plasma Physics and Controlled Fusion 53 (2010) 014011, http://dx.doi.org/10.1088/0741-3335/53/1/014011.

[16] T. Ceccotti, A. Lévy, H. Popescu, F. Réau, P. D'Oliveira, P. Monot, J.P. Geindre, E. Lefebvre, P. Martin, Physical Review Letters 99 (2007) 185002, http://dx.doi.org/10.1103/PhysRevLett.99.185002.

[17] T. Ceccotti, V. Floquet, A. Sgattoni, A. Bigongiari, O. Klimo, M. Raynaud, C. Riconda, A. Heron, F. Baffigi, L. Labate, L.A. Gizzi, L. Vassura, J. Fuchs, M. Passoni, M. Květon, F. Novotny, M. Possolt, J. Prokůpek, J. Proška, J. Pšikal, L. Štolcová, A. Velyhan, M. Bougeard, P. D'Oliveira, O. Tcherbakoff, F. Réau, P. Martin, A. Macchi, Physical Review Letters 111 (18) (2013) 185001, http://dx.doi.org/10.1103/PhysRevLett.111.185001.